

# Solution of the inverse problem of magnetic induction tomography based on Helmholtz coil

eISSN 2051-3305

Received on 18th July 2018

Accepted on 26th July 2018

E-First on 31st October 2018

doi: 10.1049/joe.2018.8286

www.ietdl.org

Hai-Jun Luo<sup>1,2</sup> ✉, Kai-Xu Wen<sup>1</sup>, Liao Yong<sup>1</sup>, Haitao Pan<sup>1</sup>, Xin Jing<sup>3</sup><sup>1</sup>College of Physics and Electronic Engineering, Chongqing Normal University, Chongqing 401331, People's Republic of China<sup>2</sup>College of Physics, Chongqing University, Chongqing 400044, People's Republic of China<sup>3</sup>Community Health Service Centers, Shuangbei, Shapingba District, Chongqing 400032, People's Republic of China

✉ E-mail: luohaijun@cqu.edu.cn

**Abstract:** Magnetic induction tomography is a contactless technique that can measure conductivity distribution in biological tissues. This study proposed that Helmholtz coils as the excitation coils will generate a set of uniform excitation fields. The system model consists of a circular background area, a circular disturbance object, a set of Helmholtz coils, and eight magnetic detection coils. The diameter of the Helmholtz coil is 200 mm. The detection coil is a square, and its side length is 12 mm. The excitation current of the system is 30 mA, and the frequency is 10 MHz. This study discusses the reconstructed images of different locations, different volumes, different distances, and different electrical conductivities of perturbation bodies. The anti-noise ability of different noise signals is also analysed. Finally, the image differences are evaluated through structural similarity index (SSIM). The results show that the algorithm can distinguish the position and volume characteristics of the target object. However, when the volume of the target object is low, the position will be deviated. This algorithm can distinguish the position of the two, which is far away from each other.

## 1 Introduction

Magnetic induction tomography (MIT) is a non-invasive and contactless measurement of biological tissue conductivity imaging technique [1–3]. MIT has multiple advantages, for example, fast, portable, low-cost, and non-invasive [4, 5]. Owing to the above features, it has a useful application prospect in the biomedical imaging, continuous and dynamic monitoring fields, especially in the continuous monitoring of intracranial diseases [6, 7]. MIT is based on Faraday's law of electromagnetic induction. The basic principle: when the alternating current flows through the exciting coil, the alternating main magnetic field ( $B_0$ ) will be generated in the space around the excitation coil. The measured object is placed under the main magnetic field, and the eddy current will be induced inside the object, thus producing the secondary magnetic field ( $\Delta B$ ) disturbing the main magnetic field. The external detection coil couples the main magnetic field and the secondary magnetic field. The disturbance of the secondary magnetic field ( $\Delta B$ ) changes to the voltage phase of the detection coil. The distribution of voltage and conductivity is closely related. The electrical conductivity distribution can be reconstructed by reconstruction algorithm [8, 9], as shown in Fig. 1.

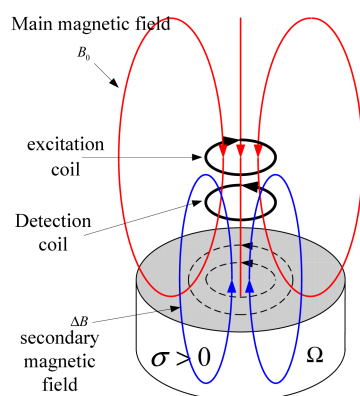


Fig. 1 Basic principle of MIT

A change of the conductivity results in an additional perturbation and the induced voltages in the detection coils include the information about the conductivity distribution, which is indispensable for the solution of the inverse problem [10]. The reconstruction algorithm of MIT mainly includes the filter back projection (FBP), sensitivity matrix, Newton step reconstruction, and tensor conductivity reconstruction algorithm. A Russian research team led by Korjenevsky developed a 16-channel closed MIT system using FBP for imaging, so as to reconstruct an image [11]. It was considered that there is a sensitive area between the detection coil and the excitation coil. Meanwhile, imaging results of different conductivity distribution conditions were obtained. The 15 differential detection coils around the hemispherical flume were reported by Xu Zheng *et al.* [12]. The 15 measurement values were projected onto the 2D plane by direct projection; meanwhile, the effects of different frequencies and two targets on the system are discussed and the results are given. Ke Li *et al.* [13] use filtered back-projection algorithm for constructing a single target and double target. In the later period, the research team uses the phase standardisation to deal with the data of each angle, which improves the resolution of the MIT FBP. This is more accurate to the target location, and the target contour is clearer [14].

The filtered back-projection algorithm follows the principle of computed tomography (CT), which linearises the magnetic force line through the object. The algorithm is characterised by fast imaging speed, but a low resolution. It is often used to detect deep, fast qualitative tests, such as real-time changes of intracranial haematoma, two-phase flow of rubber pipes etc.

In this paper, an MIT simulation model based on the Helmholtz coil is established, and the conductivity distribution of the simulation model is reconstructed by the FBP algorithm. This paper discusses the reconstructed images of different locations, different volumes, different distances, and different electrical conductivities of perturbation bodies. The anti-noise ability of different noise signals is also analysed. Finally, using the commonly used visual perception index structural similarity (SSIM) in artificial intelligence (AI), we evaluate the image difference through SSIM index. The data obtained in this paper is real and reliable by simulation software.

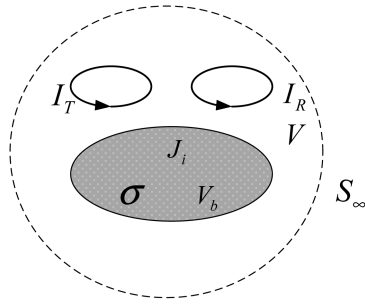


Fig. 2 Principle diagram of reciprocity theorem

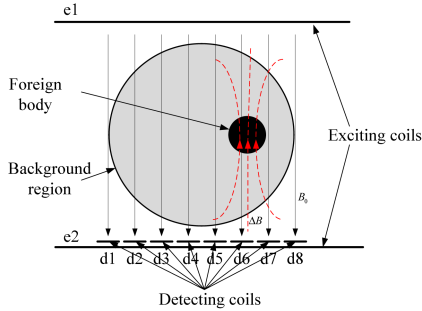


Fig. 3 Based on the Helmholtz coil of MIT system model

## 2 Method

### 2.1 Theory

MIT detects the eddy field produced by the alternating magnetic field within the conductor. The phasor form of the Maxwell equations is given below (assuming that the medium in the field is linear isotropic, passive, and non-magnetic) [15]:

$$\begin{cases} \nabla \times \mathbf{E} = -j\omega\mathbf{B} \\ \nabla \times \mathbf{H} = \mathbf{J} + j\omega\epsilon\mathbf{E} \\ \nabla \cdot \mathbf{B} = 0 \\ \nabla \cdot \mathbf{E} = 0 \end{cases} \quad (1)$$

where  $\sigma$  is the conductivity,  $\epsilon$  is the permittivity, and  $\omega$  is the angular frequency.

The measured object can be expressed as a complex conductivity  $\gamma = \sigma + j\omega\epsilon$ . According to the Maxwell equations of the harmonic magnetic field, the system working frequency of 10 MHz, leading to the real part that causes the complex conductivity of the material is much larger than the imaginary part ( $\sigma \gg \omega\epsilon$ ). Therefore, when deducing the governing equation, the MIT theory ignores the influence of the dielectric constant of the conductive region, that is, the displacement current is not considered [16]:

$$\frac{1}{\mu} \nabla^2 \mathbf{A} - j\omega\sigma\mathbf{A} = -\mathbf{J}_T \quad (2)$$

where  $\mathbf{A}$  is the magnetic vector potential in space,  $\mathbf{J}_T$  is the current density distributed in the excitation coil. According to (1) the Maxwell equations and assumptions, (2) can be derived. Equation (2) establishes the relationship between the space magnetic vector level, the conductivity of the measured object, and the excitation current. However, in the actual measurement system of MIT, the relationship between the distribution of electrical conductivity and the change of detection voltage is mainly studied. In order to establish the theoretical relationship between induced voltage variation and electrical conductivity, according to the reciprocity theorem, the principle diagram of the reciprocity theorem is shown in Fig. 2.

The expression of flux in the detection coil is first established as [17]

$$\Phi = \frac{1}{I_R} \int \mathbf{A}_R \cdot \mathbf{J} \cdot d\mathbf{V} \quad (3)$$

where  $I_R$  is the reciprocal current through detecting coil,  $\mathbf{A}_R$  is the magnetic vector potential of the reciprocal current.  $\mathbf{J}$  includes two parts of current density: one is the current density in the excitation coil, which is expressed in  $\mathbf{J}_T$ , the other is the current density of the eddy current induced by the target object, which is expressed in  $\mathbf{J}_i$ . So, formula (3) can be decomposed into the following equation:

$$\Phi = \frac{1}{I_R} \int \mathbf{A}_R \cdot \mathbf{J}_T \cdot dV_{\text{coil}} + \frac{1}{I_R} \int \mathbf{A}_R \cdot \mathbf{J}_i \cdot dV_b \quad (4)$$

where  $V_{\text{coil}}$  is the volume of the excitation coil and  $V_b$  is the volume of the target object. The first item on the right side of (4) means the magnetic flux of the excitation fields in the detection coil, and the second item means the magnetic flux of the induced magnetic fields in the detection coil. According to the upper equation (4) excitation magnetic field and the secondary magnetic field in detecting the magnetic flux in the coil, the induced voltage of the excitation magnetic field and the secondary magnetic field can be derived, respectively, as shown in the following equation:

$$v = -j\omega\Phi = -j \left( I_T \oint \left( \frac{\omega\mathbf{A}_R}{I_R} \right) \cdot d\mathbf{l} \right) - \int \left( \frac{\omega\mathbf{A}_R}{I_R} \right) \times \sigma(\omega\mathbf{A}_T + \nabla\varphi) dV_b \quad (5)$$

where  $\mathbf{A}_T$  is the magnetic vector potential of this excitation current. The induced voltage is a complex number, in which the real part is the voltage induced by the secondary magnetic field on the detection coil, and the virtual part is the voltage induced by the main magnetic field on the detection coil. Therefore, the two parts of the induction voltage phase difference is  $90^\circ$ .

### 2.2 Modelling

This paper uses the FBP algorithm to reconstruct the image. The data of the FBP algorithm comes from the eight-channel revolving MIT simulation model. The experimental model of MIT based on Helmholtz coil is shown in Fig. 3. The MIT simulation model is composed of a cylindrical background region, a cylindrical interference object, a set of Helmholtz coils (e1, e2), and eight square detection coils (d1–d8). The eight detection coils are in the same plane as one of the groups of Helmholtz coils.

As is shown in Fig. 3, the main magnetic field ( $B_0$ ) is generated by the excitation current through a set of Helmholtz coils (e1, e2). When the excitation magnetic penetration of background objects and disturbance objects, eddy current induced inside the object will generate secondary magnetic field ( $\Delta B$ ). The synthesised field ( $B_0 + \Delta B$ ) of the primary and secondary magnetic field will be measured on the detection coils.

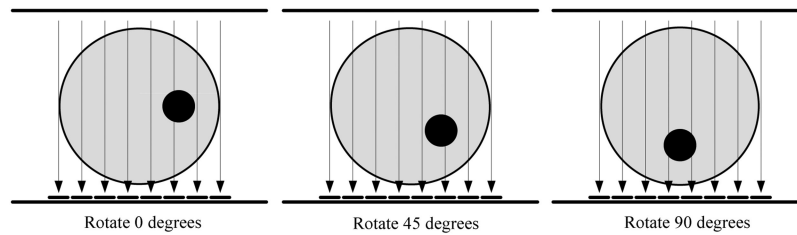
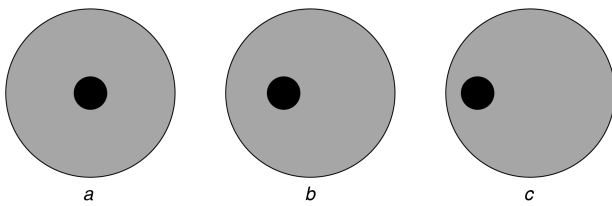
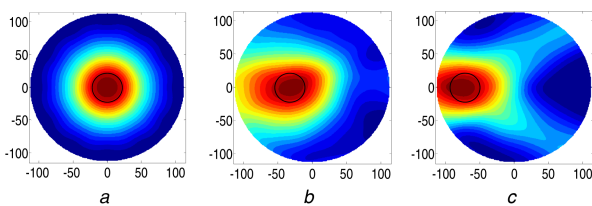
In this paper, we use the electromagnetic simulation software to establish the eight-channel magnetic induction rotation measurement system simulation model, as shown in Fig. 3. The model parameters are given in Table 1. The radius of the Helmholtz coil is 100 mm, and the distance between two Helmholtz coils is 100 mm. The length of each detection coil is 12 mm, and each detection coil is at a distance of 1 mm. The diameter of the background is 90 mm. The diameter of the disturbance body is 15 mm, and its height is 40 mm. The electrical conductivity of the background object is 0.2S/m, and the conductivity of the disturbance body is 2 S/m. The excitation current is 30 mA, and the excitation frequency is 10 MHz.

According to the FBP algorithm, the detection system should revolve around the measured object. In this research, the excitation coils and the magnetic test coils are fixed for the convenience of the system experiment. The object revolves around its own central point. As shown in Fig. 4, the schematic diagram of the three positions after the rotation of the object is briefly described.

Since the volume of the disturbance object is far smaller than that of the background region, the induction voltage generated is

**Table 1** System model parameters

	Det-coil	Exc-coil	Background	Disturbance
size, mm	length 12 mm	diameter 200 mm	diameter 90 mm	diameter 15 mm
conductivity	copper	copper	0.2S/m	2S/m
current		30 mA		
frequency		10 MHz		

**Fig. 4** Schematic of MIT system rotation model**Fig. 5** Models of the perturbation objects on the three different positions  
(a) In the centre, (b) 15 mm away from the centre, and (c) 30 mm away from the centre**Fig. 6** Image results of the perturbation objects on the three different positions  
(a) In the centre, (b) 15 mm away from the centre, and (c) 30 mm away from the centre

far smaller than that by the background region. This makes static imaging difficult. Thus, dynamic imaging is adopted in this research. Dynamic imaging steps are shown below:

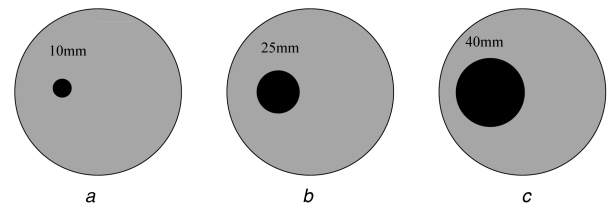
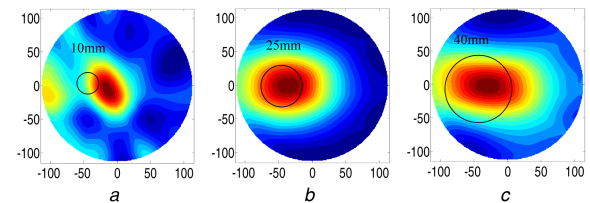
- Set the conductivity of the disturbance object and the background region to be 0.2S/m, rotate the object to be tested by one circle at the stepping of  $30^\circ$  to obtain a group of voltage values. Every group has eight voltage values. Finally, ' $12 \times 8$ ' voltage values will be obtained. These data should be saved as the benchmark data for the dynamic measurement.
- Set the conductivity of the disturbance object to be 2S/m and the conductivity of the background region to be 0.2S/m. Like the above step, eventually, ' $12 \times 8$ ' voltage values can be obtained.
- Find the difference between the two measurement data and normalise them. Use the difference to restructure the conductivity distribution of the object by the back-projection algorithm.

### 3 Results

In order to illustration the realisation process of the MIT algorithm based on the Helmholtz coils, some simple examples are adopted. The effect of reconstruction algorithm in the different models and its noise suppression ability was tested.

#### 3.1 Target position change imaging

As shown in Fig. 5, the perturbation objects have three different positions. The conductivity of the disturbance objects and the

**Fig. 7** Diagram of the different size of perturbation objects  
(a) The diameter 10 mm, (b) the diameter of 20 mm, and (c) the diameter of 40 mm**Fig. 8** Image results of the two different sizes of perturbation objects  
(a) The diameter 10 mm, (b) the diameter 20 mm, and (c) the diameter 40 mm

background region are set to be 2 and 0.2S/m, respectively. The diameter of the disturbance object is placed at 15 mm. Fig. 5a shows that the disturbance object is in the centre of the background region. Fig. 5b shows that the disturbance object is 15 mm away from the centre. Fig. 5c shows that the disturbance object is about 30 mm away from the centre.

Rotate the object to be tested at the stepping of  $30^\circ$  to obtain ' $12 \times 8$ ' voltage values. According to the above method, the benchmark data of the simulation model is obtained. Find the difference between the data of three models and the benchmark data. FBP algorithm is adopted in order to obtain the imaging result shown in Fig. 6.

According to Fig. 6, the position of the target object can be accurately located, but the size of image is larger than that of the actual perturbation object. Since only eight magnetic detection coils are adopted in the experimental system, the size of coils might result in the positional deviation of objects. If the size of coils is reduced, the positioning of the target can be more precise.

#### 3.2 Target volume change imaging

The three simulation models of the disturbance object of different volumes are built in the background region. As shown in Fig. 7, the diameters of the three disturbance objects are 10, 25, and 40 mm. The conductivity of the disturbance object is 2S/m. ' $12 \times 8$ ' voltage values are obtained. According to the above method, the imaging results are shown in Fig. 8.

According to Fig. 8, the imaging results can basically reflect the volume size of the target. In Fig. 8a, the imaging of the object is obviously smaller than that of the latter two models. In Fig. 8b, the imaging of the object with a diameter of 25 mm is also smaller than



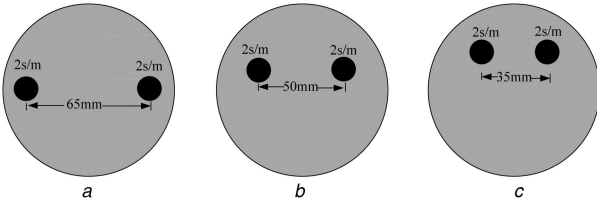


**Fig. 9** Models of the two same perturbation objects locate in different positions  
(a) The distance is 65 mm, (b) this distance is 50 mm, and (c) this distance is 35 mm

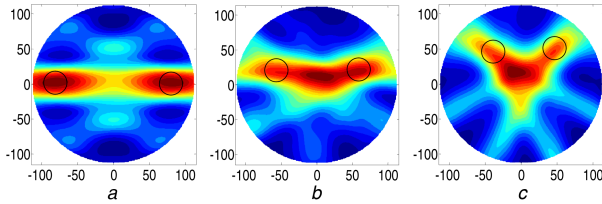


**Fig. 10** Image results of the two same size and conductivity perturbation objects locate in different distance  
(a) The distance is 65 mm, (b) the distance is 50 mm, and (c) the distance is 35 mm

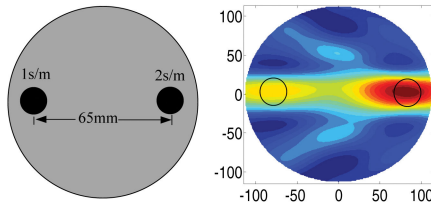


**Fig. 11** Model and image of two different conductivity perturbation objects

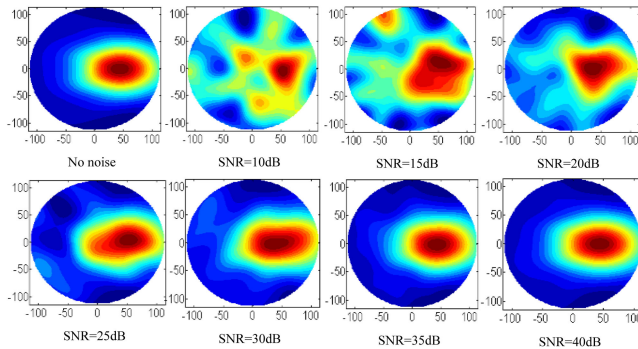


**Fig. 12** Image results of the different SNR

that with a diameter of 40 mm. This shows that the volume of the target object can exert some influence on the imaging effect. However, due to the bending of the induced magnetic line, the size of the coils, and the weak characteristic of the secondary magnetic field, the position of the small target object with a diameter of 10 mm might deviate. Artefacts of the other accompanying disturbances appear.

### 3.3 Bi-target imaging

Three simulation models are built according to the above model data. In Fig. 9, the conductivity of two disturbance objects is 2S/m and that of the background is 0.2S/m. The diameter of the two disturbance objects is 15 mm, and the distances of the two objects are 65, 50, and 35 mm.

From Fig. 10a, it can be seen that, when two objects are 65 mm away from each other, the position of the two objects can be distinguished, but there are fewer artefacts in the centre. When two objects are away from each other by 50 and 35 mm, As shown in Figs. 10b and c, the images of the two target objects are mixed together. Analysis of the reasons are as follows: due to the bending magnetic line of force of the eddy field, the secondary magnetic field generated by the eddy is received not only by the coils of the

sensors at the top of the objects, but also by the coils of the adjacent opposite sensors. If the two target objects are near to each other, the magnetic detection coils in the centre can receive the superposition of the eddy field from the two objects. Therefore, the signal of coils in the middle is stronger than that of the coils above the target objects. Therefore, when the distance between two target objects is relatively short, the algorithm cannot be separated from the two target objects.

In Fig. 11, the conductivities of the two disturbance objects are 2 and 1S/m. The diameter of the two disturbance objects is 15 mm. The centre of the disturbance objects is 65 mm away from each other. The simulation model of the benchmark data is built through the above method to obtain the benchmark data. Find the difference between the data of three models and the benchmark data. The FBP algorithm is adopted to obtain the imaging result shown in Fig. 11.

As shown in Fig. 11, when the two target objects are relatively far away from each other, the imaging results of the disturbance objects with different conductivities can be basically distinguished. The imaging results are different in terms of colour. The disturbance object with a higher conductivity is red; while the one with a lower conductivity is yellowish.

### 3.4 Noise suppression ability

The research data are simulated under the ideal situation, and the imaging results are obtained free from the noise disturbance. However, in the practical MIT imaging system, there are various noise factors. In the following section, the Gaussian noise, (signal noise ratio) SNR = 10 dB, SNR = 15 dB, SNR = 20 dB, SNR = 25 dB, SNR = 30 dB, SNR = 35 dB, and SNR = 40 dB, are added into the voltage value to be measured in the simulation calculation. The image obtained through the image restructuring of the simulation model through the algorithm is shown in Fig. 12.

The comparison of the imaging results with noise and without noise shows that the algorithm has favourable noise immunity. When the SNR is 10 dB, the image can display the general region of the perturbation object. However, in the other regions, there are some shadows. When the SNR is 15 dB, the shadows of the other regions are fewer. When the SNR is 20 dB, the image is basically clearly displayed, but the shape is not good enough. When the SNR is above 25 dB, the image is clearly displayed, the shape is good and there is almost no disturbance around.

## 4 Image quality assessment (IQA) algorithm

IQA research aims to provide objective measures that can automatically predict the perceived image quality. An IQA measure can play an important role in a large number of image processing applications, for algorithm optimisation and benchmarking purposes [18].

SSIM is a way to measure the subjective quality of television, film, or other digital images and videos. AI and machine learning are changing all this by mastering non-reference picture quality assessment. AI uses a wide range of function sets and learning from error patterns can provide near real-time quality assessment, and SSIM is one of the most extensive visual perception indicators. The system diagram of the proposed quality assessment system is shown in Fig. 13. Suppose  $x$  and  $y$  are two nonnegative image signals, which have been aligned with each other (e.g. spatial patches extracted from each image) [18]

$$\text{SSIM}(x, y) = \frac{(2\mu_x\mu_y + C_1)(2\sigma_{xy} + C_2)}{(\mu_x^2 + \mu_y^2 + C_1)(\sigma_x^2 + \sigma_y^2 + C_2)} \quad (6)$$

$$\mu_x = \frac{1}{N} \sum_{i=1}^N x_i \quad (7)$$

$$\mu_y = \frac{1}{N} \sum_{i=1}^N y_i \quad (8)$$

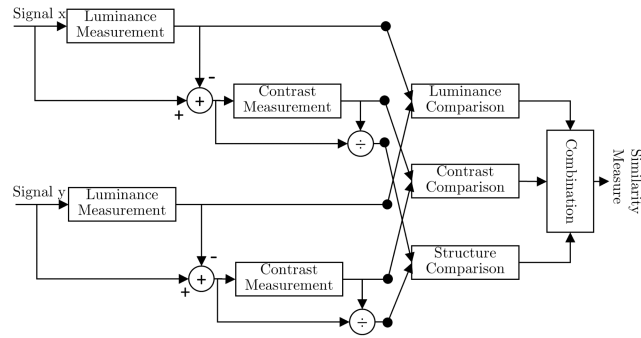


**Fig. 13** Diagram of SSIM measurement system

**Table 2** SSIM of the different noise

SNR	10 dB	15 dB	20 dB	25 dB	30 dB	35 dB	40 dB					
SSIM	0.7900	0.8237	0.8438	0.8550	0.8765	0.8612	0.8980	—	—	—	—	—

**Table 3** SSIM of the different positions

Distance to centre	0 mm	15 mm	30 mm
SSIM	0.8513	0.8510	0.8897

**Table 4** SSIM of the different diameter

Diameter	10 mm	20 mm	40 mm
SSIM	0.8396	0.8272	0.8105

**Table 5** SSIM of the distance to bi-target

Distance to bi-target	65 mm	50 mm	35 mm
SSIM	0.8438	0.8313	0.8348

$$\sigma_x = \left( \frac{1}{N-1} \sum_{i=1}^N (x_i - \mu_x)^2 \right)^{1/2} \quad (9a)$$

$$\sigma_y = \left( \frac{1}{N-1} \sum_{i=1}^N (y_i - \mu_y)^2 \right)^{1/2} \quad (9b)$$

$$\sigma_{xy} = \frac{1}{N-1} \sum_{i=1}^N (x_i - \mu_x)(y_i - \mu_y) \quad (10)$$

where  $\mu_x$  is the average of  $x$ ,  $\mu_y$  is the average of  $y$ ,  $\sigma_x^2$  is the variance of  $x$ ,  $\sigma_y^2$  is the variance of  $y$ ,  $\sigma_{xy}$  is the covariance of  $x$  and  $y$ ,  $C_1 = (k_1 L)^2$  and  $C_2 = (k_2 L)^2$  are used to maintain a constant,  $L$  is the dynamic range of pixel values. The SSIM ranges from  $-1$  to  $1$ . When the two images are the same, the value of SSIM is equal to  $1$ . From Table 2, it can be seen that with the increase of SNR, the image is closer to the real image.

From Tables 3–5, we can see that the imaging results from the edge are better. Small diameter imaging results are close to true distribution. The imaging results of two objects far away are better.

## 5 Discussions

This paper conducts a detailed description of the principle and realisation of FBP algorithm for the MIT based on the Helmholtz coils. The basic idea of the computer's tomography is applied to the MIT. This paper comes to the following conclusions as to FBP algorithm for the MIT.

(i) FBP algorithm for MIT can distinguish the position and volume characteristics of the target object. However, when the volume of the target object is small, the position will be deviated and the other accompanying artefacts appear.

(ii) The detected objects have multiple objects. When the target objects are far away from each other, the position of the two can be distinguished, but there are some artefacts in between. However, when the target objects are close to each other, they cannot be separated and are mixed.

(iii) The noise immunity test of the FBP algorithm is conducted by adding the Gaussian noise. The different noises are added into the voltage value to be measured in the simulation calculation. The image obtained through the image restructuring of the simulation model through the algorithm. When the SNR is above 25 dB, the image is clearly displayed, the shape is good and there is almost no disturbance around. The comparison of the imaging results with noise and without noise shows that the algorithm has favourable noise suppression ability.

## 6 Acknowledgments

This work was supported by the National Natural Science Foundation of China (grant no. 51507023), and Natural Science Foundation Project of CQ CSTC (grant no. CSTC2016JCYJA0920), and the Science and Technology Research Program of Chongqing Municipal Education Commission (grant no. KJ1703063).

## 7 References

- [1] Griffiths, H., Stewart, W. R., Gough, W.: 'Magnetic induction tomography. A measuring system for biological tissues', *Ann. New York Acad. Sci.*, 1999, **873**, (1), pp. 335–345
- [2] Li, F., Abascal, J.F.P.J., Desco, M., *et al.*: 'Total variation regularization with split Bregman-based method in magnetic induction tomography using experimental data', *IEEE Sens. J.*, 2017, **17**, (4), pp. 976–985
- [3] Hollaus, K., Magele, C., Merwa, R., *et al.*: 'Numerical simulation of the eddy current problem in magnetic induction tomography for biomedical applications by edge elements', *IEEE Trans. Magn.*, 2004, **40**, (2), pp. 623–626
- [4] Watson, S., Williams, R.J., Gough, W., *et al.*: 'A magnetic induction tomography system for samples with conductivities below 10S/m', *Meas. Sci. Technol.*, 2008, **19**, (4), pp. 88–91

- [5] Luo, H.J., He, W., Xu, Z., *et al.*: 'Preliminary results on brain monitoring of meningitis using 16 channels magnetic induction tomography measurement system', *Prog. Electromagn. Res.*, 2012, **M24**, (3), pp. 57–68
- [6] Chen, Y. Y., Xu, W., Yi, L., *et al.*: 'Analysis of sensitivity characteristic and image reconstruction for brain magnetic induction tomography', *J. Northeastern Univ.*, 2012, **33**, (6), pp. 782–785
- [7] Xiao, Z., Tan, C., Dong, F.: 'Brain tissue based sensitivity matrix in hemorrhage imaging by magnetic induction tomography'. IEEE Int. Instrumentation and Measurement Technology Conf., Torino, Italy, 2017, pp. 1–6
- [8] Korjenevsky, A., Cherepenin, V., Sapetsky, S.: 'Magnetic induction tomography: experimental realization', *Physiol. Meas.*, 2000, **21**, (1), pp. 89–94
- [9] Ma, L., Hunt, A., Soleimani, M.: 'Experimental evaluation of conductive flow imaging using magnetic induction tomography', *Int. J. Multiph. Flow*, 2015, **72**, (20), pp. 198–209
- [10] Hintermüller, M., Laurain, A., Youssef, I.: 'Shape sensitivities for an inverse problem in magnetic induction tomography based on the eddy current model', *Inverse Probl.*, 2015, **31**, (6), pp. 1–25
- [11] Korjenevsky, A. V., Sapetsky, S.: 'Feasibility of backprojection method for reconstruction of low contrast perturbations in a conducting background in magnetic induction tomography', *Physiol. Meas.*, 2017, **38**, (6), pp. 1204–1213
- [12] Xu, Z., Luo, H.J., He, W., *et al.*: 'A multi-channel magnetic induction tomography measurement system for human brain model imaging', *Physiol. Meas.*, 2009, **30**, (6), pp. 175–186
- [13] Li, K., Xiao, L., Qiang, D., *et al.*: 'Research on dynamic image reconstruction for MIT based on back-projection algorithm', *Chin. J. Sci. Instrum.*, 2013, **34**, (2), pp. 394–400
- [14] Ke, L., Cao, F., Du, Q.: 'Back-projection matrix calculation and data processing methods used in magnetic induction tomography', *Chin. J. Sci. Instrum.*, 2014, **35**, (10), pp. 2256–2262
- [15] He, W., Luo, H.J., Xu, Z., *et al.*: 'Multi-channel magnetic induction tomography measurement system', Int. Conf. on Biomedical Engineering and Informatics. IEEE, Yantai, China, 2010, pp. 402–405
- [16] Luo, H., He, W., Xu, Z., *et al.*: 'The filtered back-projection algorithm of magnetic induction tomography with uniform magnetic excitation', *J. Chongqing Univ.*, 2013, **36**, (3), pp. 77–81
- [17] Haijun, L., Xin, J.: 'The magnetic induction tomography measurement system based on Helmholtz coil'. 2015 8th Int. Conf. on Biomedical Engineering and Informatics (BMEI), Shenyang, China, 2015
- [18] Wang, Z., Bovik, A. C., Sheikh, H. R., *et al.*: 'Image quality assessment: from error visibility to structural similarity', *IEEE Trans. Image Process.*, 2004, **13**, (4), pp. 600–612